Fuel 398 (2025) 135598

Contents lists available at ScienceDirect

Fuel

journal homepage: www.elsevier.com/locate/jfue

Full Length Article

On nanoparticles in iron dust flames of Bunsen-type: Evolution of size distribution and hetero-coagulation with micron-sized particles

Fabian P. Hagen[a,*], Jonas H. Müller[a], Heike Störmer[b], Björn Stelzner[a], Yolita M. Eggeler[b], Dimosthenis Trimis[a]

[a] Karlsruhe Institute of Technology (KIT), Engler-Bunte-Institute, Combustion Technology, Karlsruhe, Germany
[b] Karlsruhe Institute of Technology (KIT), Laboratory for Electron Microscopy, Karlsruhe, Germany

HIGHLIGHTS

- On-line particle probing and mobility sizing reveal nanoparticle size evolution.
- Nanoparticle size distribution broadens due to condensation-driven growth.
- Hetero-coagulation with micron-sized particles reduces gas-borne nanoparticles.
- Increased oxygen concentrations enhance nanoparticle formation.
- Equivalence ratio affects nanoparticle formation and (hetero-)coagulation.

ARTICLE INFO

Keywords:
Nanoparticle size distribution
Laminar iron dust flame
On-line particle probing
Differential mobility sizing
Electron microscopy
Hetero-coagulation

ABSTRACT

This study investigates the evolution of nanoparticle size distributions in laminar iron dust flames of Bunsen-type as a function of equivalence ratio, oxygen concentration in the oxidizer, and the size distribution of seeded micron-sized particles. Experiments were conducted using a Bunsen-type burner. Spatially resolved nanoparticle size distributions were measured via on-line particle probing and differential mobility sizing. Thermophoretic sampling enabled morphology and phase analysis via scanning and transmission electron microscopy (SEM and TEM) and energy-dispersive X-ray (EDX) spectroscopy. Nanoparticles form in the boundary layer of burning micron-sized particles and are transported into the surrounding gas phase, where they undergo condensation-driven growth, leading to a broadening of their size distribution along the flame axis. The mobility size distribution, which includes both single nanoparticles and aggregates, shifts toward larger sizes, while the number concentration decreases due to coagulation. Hetero-coagulation with micron-sized particles leads to the formation of nanoparticle coatings on their surfaces, reducing the fraction of gas-borne nanoparticles. At the flame tip, higher equivalence ratios, elevated oxygen concentrations, and smaller seeded particles increase nanoparticle number concentrations. Additionally, smaller seeded iron particles result in a narrower nanoparticle size distribution. Further downstream, hetero-coagulation dominates over nanoparticle growth, leading to a continuous reduction in the gas-borne nanoparticle volume fraction. These findings indicate that mitigation strategies could be based on controlling hetero-coagulation, adjusting the oxygen concentration in the oxidizer, or carefully selecting the equivalence ratio and/or the size distribution of micron-sized iron particles.

1. Introduction

Micron-sized iron particles are promising candidates as a carbon-free energy carrier for renewable hydrogen storage [1–4]. Green hydrogen reduces iron oxide to iron, storing renewable energy. The resulting iron particles serve as a solid fuel with high volumetric energy density, enabling energy release through combustion. A key challenge in the combustion of micron-sized particles is the formation of nanoparticles [5]. During high-temperature oxidation, micron-sized iron particles can partially melt and vaporize, leading to localized supersaturation of iron

* Corresponding author.
Email address: fabian.hagen@kit.edu (F.P. Hagen).

https://doi.org/10.1016/j.fuel.2025.135598
Received 25 February 2025; Received in revised form 21 April 2025; Accepted 4 May 2025
Available online 8 May 2025

vapor in the boundary layer, i.e., in the surrounding gas phase. Either through reaction-driven nucleation via oxidation or homogeneous nucleation, liquid iron and/or iron oxide nanodroplets or solid nanoparticles can form, coalesce, undergo a phase transition, grow in size, and coagulate either among themselves or with micron-sized parent particles. Their formation complicates post-combustion handling, as their small size makes separation challenging and may impair recyclability [6,7].

Previous experimental studies consistently report the formation of iron oxide nanoparticles during iron particle combustion. In single-particle combustion experiments, Ning et al. [8–10] demonstrated that maximum particle temperature depends on oxygen concentration, with nanoparticle formation occurring even below the boiling points of iron and iron oxides. Similarly, Li et al. [11] and Panahi et al. [12] observed a nanoparticle aerosol cloud surrounding micron-sized iron particles during single particle combustion. In entrained-flow experiments, i.e., iron dust flames, Li et al. [13] and Tóth et al. [14], also reported on nanoparticle formation. Collectively, these findings highlight the critical role of oxygen concentration and particle temperature in nanoparticle formation across different combustion setups. While these studies provide valuable insights into qualitative nanoparticle concentration during formation, they do not yet resolve questions regarding nanoparticle size, its evolving distribution, or interactions with parent micron-sized particles.

Two pathways for nanoparticle formation have been proposed. Thijs et al. [15] assumed, due to uncertainties in molecular level formation mechanisms, that Fe_2O_3 nanoparticles result from the rapid conversion of FeO_2(g), which forms through the oxidation of Fe(g). While experimental data support the assumption that Fe_2O_3 dominates in collected nanoparticle samples [5,12,14,16], the actual oxide phase of nanoparticles near a combusting micron-sized particle may differ. In contrast to [15], Li et al. [17] recently proposed that nanoparticles form through clustering of iron and iron oxide molecules, with FeO as the predominant phase at temperatures above 2000 K. This is supported by the fact that, according to the phase diagram, Fe_2O_3 is stable only at <1700 K [18], a temperature that is exceeded during nanoparticle formation [9,11]. Based on these findings, Nguyen et al. [19] developed a model in which supersaturated Fe(g) and FeO(g) vapor condenses into liquid nanodroplets. Their simulations, along with corresponding experimental results from single particle oxidation experiments by Li et al. [17,20], highlight again that temperature of micron-sized particles is critical for nanoparticle formation. Furthermore, it is concluded that convection and thermophoresis are the key transport processes in the nanoparticle aerosol surrounding the parent micron-sized particles, while nanoparticle diffusion plays a minor role. The formed nanoparticle volume fraction is similar for the mechanism proposed by Thijs et al. [15] and homogeneous nucleation [19], with the latter being largely insensitive to gas-phase reactions.

Given the lack of validation data on the evolution of nanoparticle size distributions during formation, it is understandable that only one of the two studies considers this aspect. While the model by Nguyen et al. [19] does not yet account for nanoparticle size distribution evolution, Thijs et al. [15] computed it using a sectional population balance model. They reported an average nanoparticle diameter of $\overline{d}_p = 50$ nm for the combustion of an iron particle of $D = 50$ µm in air. This value was confirmed by the *ex situ* analysis of a micron- and nano-sized particles collected post-flame from a stoichiometric iron dust flame seeded with a smaller particle ensemble with $D_{50} = 18$ µm [21].

To address existing gaps in validation data and provide insights into nanoparticle evolution in laminar iron dust flames, this study focuses on two key aspects:

i. The evolution of nanoparticle size distributions in the post-reaction zone of laminar iron dust flames via spatially resolved measurements.
ii. The hetero-coagulation of nanoparticles with micron-sized parent particles to assess the impact on the evolution of the nanoparticle size distribution.

These two aspects are analyzed as a function of the equivalence ratio, the size distribution of micron-sized particles, and the molar oxygen concentration in the oxidizer. For these experiments, the iron dust burner of Bunsen-type introduced by Fedoryk et al. [22] is employed. This burner enables the stabilization of self-sustained laminar iron dust flames, providing a well-defined environment for systematic parameter variation. Spatially resolved nanoparticle size distributions are measured using on-line particle probing and differential mobility sizing, while thermophoretic sampling combined with scanning electron microscopy, transmission electron microscopy (SEM and TEM), and energy-dispersive X-ray (EDX) spectroscopy provides insights into nanoparticle oxide phases and their coagulation dynamics with micron-sized particles.

2. Theoretical approach and terminology

The formation of nanoparticles during the combustion of micron-sized iron particles follows a sequence of consecutive steps, as depicted in Fig. 1. The starting point of nanoparticle formation is iron vapor in the boundary layer of a burning particle, released through vaporization driven by high surface temperatures. The subsequent formation of nanodroplets may occur via two mechanisms, neglectingven clustering:

- Reaction-driven nanodroplet formation. Nanodroplets can form when iron vapor oxidizes, forming iron oxides with a significantly lower saturation vapor pressure. This sudden reduction in saturation vapor pressure leads to local supersaturation, triggering the immediate nucleation of liquid iron oxide nanodroplets [23,24].
- Homogeneous nucleation. Nanodroplets can form via the spontaneous clustering of atoms when the vapor pressure of iron exceeds its equilibrium saturation pressure leading to spontaneous, homogeneous nucleation and the formation of nanodroplets. The critical size for stable clusters, d_d^{crit}, is governed by the Kelvin equation [25–27].

Nanodroplets with the critical size d_d^{crit}, estimated to be in the range of approx. 1 nm [28], with the exact value depending on boundary conditions, form by either mechanism can grow in size via coalescence or condensation, see Fig. 1:

- Nanodroplet coalescence. The merging of nanodroplets increases their volume, resulting in a larger droplet diameter [23].
- Nanodroplet growth by condensation. If the gas phase surrounding the nanodroplet is supersaturated, iron or iron oxide vapor condenses continuously, increasing the size of the nanodroplet. In contrast to homogeneous nucleation, which requires overcoming a critical energy barrier for cluster formation, condensation onto an existing droplet is thermodynamically favorable and continues as long as supersaturation is maintained [27,29].

As shown by Finke and Sewerin [30], the predicted evolution of the nanodroplet distribution during single aluminum particle combustion—accounting for condensational growth and coalescence—reveals how these processes gradually shift the initially narrow size distribution [31] toward a self-preserving log-normal distribution [32]:

$$P(d_i) = \frac{1}{\sqrt{2\pi}\, d_i\, \ln(\sigma_{g,i})} \exp\left[-\frac{1}{2}\frac{[\ln(d_i) - \ln(\overline{d}_i)]^2}{\ln^2(\sigma_{g,i})}\right]. \quad (1)$$

Here, $\overline{d}_i$ represents the count median diameter (CMD), while $\sigma_{g,i}$ denotes the geometric standard deviation (GSD) of the log-normally distributed but unspecified diameter d_i. For example, in the case mentioned above, $\sigma_{g,i}$ shifts from approx. 1.20 to 1.46, representing the self-preserving limit for spheres in the free molecular regime [33].

The phase transition from nanodroplets to solid nanoparticles is a critical step in the formation sequence, occurring at different times depending on temperature and pressure [29]. As a result, the distinction between liquid nanodroplets and solid nanoparticles is inherently diffuse, and the transition can start immediately after droplet formation

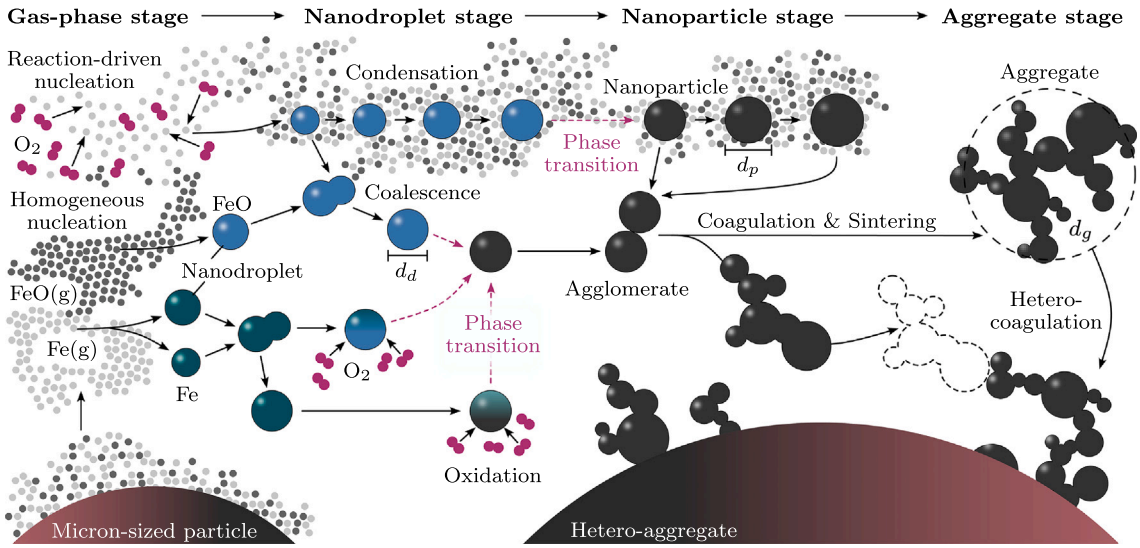

Fig. 1. Overview of the multiple pathways in the nanoparticle formation sequence occurring simultaneously.

or even bypass the liquid state entirely. In general, solidification occurs once the temperature drops below the melting point. However, due to the Gibbs–Thomson effect, nanodroplets exhibit a size-dependent melting point depression [34], which hinders solidification even at temperatures where bulk material would be solid. Conversely, reaction-driven nanoparticle formation can lead to the immediate formation of solid iron oxide nanoparticles without passing through a liquid state. Consequently, the phase transition is not a discrete event but an inherent and continuous process throughout nanoparticle formation and evolution.

Similar to nanodroplets, solid nanoparticles undergo surface growth via condensation. The size distribution of solid nanoparticles can be described by a log-normal distribution, as given in Eq. (1). In this case, the unspecified CMD, $\overline{d}_i$, and GSD, $\sigma_{g,i}$, correspond to the nanoparticle diameter d_p and geometric standard deviation $\sigma_{g,p}$, respectively. Here, it should be noted that it will be shown that the nanoparticles formed and sampled from iron dust flames are not spherical. Therefore, d_p refers to the projected area equivalent primary nanoparticle diameter in the following.

While the correct notation for nanodroplets would be d_d and $\sigma_{g,d}$, this distinction is not relevant in the present study, as only solid nanoparticles can be analyzed due to particle probing from the flame. Nonetheless, it is crucial to distinguish between nanodroplets and nanoparticles, as their collision dynamics differ fundamentally: when two nanodroplets collide, they coalesce. In contrast, the collision of two nanoparticles leads to coagulation, forming loosely bonded agglomerates and—in combination with sintering—fractal aggregates, see Fig. 1.

Within the aggregates, nanoparticles are firmly bonded by sintering bridges [35]. The geometric size of the aggregates is quantified by the diameter of gyration d_g, defined as twice the more commonly used radius of gyration, i.e., twice the mean distance of the i-th nanoparticle from the aggregate's center of mass [36]. The formation of these fractal aggregates, driven by coagulation and sintering, asymptotically approaches a self-sustaining log-normal size distribution, referred to as $P(d_g)$, see Eq. (1). The number of primary particles per aggregate N_p scales with the ratio of the diameter of gyration to the nanoparticle diameter, following a power law [36]:

$$N_p = k_f \left(\frac{d_g}{d_p}\right)^{D_f}. \tag{2}$$

D_f describes the fractal dimension of the aggregate and ranges between $1 \leq D_f \leq 3$. For a linear particle chain, the fractal dimension is equal to one, while a densely packed spherical aggregate corresponds to $D_f = 3$. Fractal structures formed by diffusion-limited cluster-cluster agglomeration (DLCA) exhibit $D_f = 1.78$, while diffusion-limited particle-cluster agglomeration (DLA) results in $D_f = 2.5$, Ballistic cluster-cluster agglomeration (BCCA) yields $D_f = 1.90$, whereas ballistic particle-cluster agglomeration (BPCA) produces compact structures with $D_f = 3.0$, as summarized by Schaefer and Hurd [37] as well as Eggersdorfer and Pratsinis [38]. The mechanism governing nanoparticle coagulation during the combustion of micron-sized iron particles is not yet resolved, but determining D_f may provide insight into the dominant agglomerate or aggregate formation process. The fractal prefactor k_f relates to the anisotropy of the fractal aggregate [35] and is linked to the fractal dimension according to Sorensen and Roberts [36]. For aggregates with $D_f = 1.6 \ldots 2.0$, k_f can be approximated as 1.2 ± 0.1 [36]. A transmission electron microscopy image of a representative aggregate with $D_f \approx 1.8$, thermophoretically sampled from a stoichiometric iron dust flame, visualizing d_p and d_g, is shown in Fig. 2.

During the combustion of micron-sized iron particles, thermophoresis primarily governs the transport of incipient nanoparticles from the boundary layer near the particle surface into the surrounding aerosol. At high surface temperatures, strong evaporation induces a Stefan flow directed outward, which further supports nanoparticle transport. The nanoparticles then encounter different coagulation partners, resulting in three possible outcomes, see Fig. 1:

- Coagulation with another single nanoparticle, leading to the formation of an agglomerate that may subsequently sinter into an aggregate.
- Coagulation with an aggregate, changing the morphology and thereby influencing D_f and/or d_g.
- Hetero-coagulation, deposition, and possibly sintering on the surface of a micron-sized parent particle.

Moreover, collisions between two aggregates or agglomerates, resulting in their coagulation, are possible.

Fig. 2 also shows the mobility diameter d_m, defined as the diameter of a sphere with the same electrical mobility as the investigated nanoparticle or aggregate. In this study, particle probing combined with differential mobility sizing enables the on-line quantification of d_m within the flame environment. The mobility diameter must be considered as follows: For single nanoparticles moving in the gas flow, the mobility diameter is approx. equal to the nanoparticle diameter, $d_m \approx d_p$,

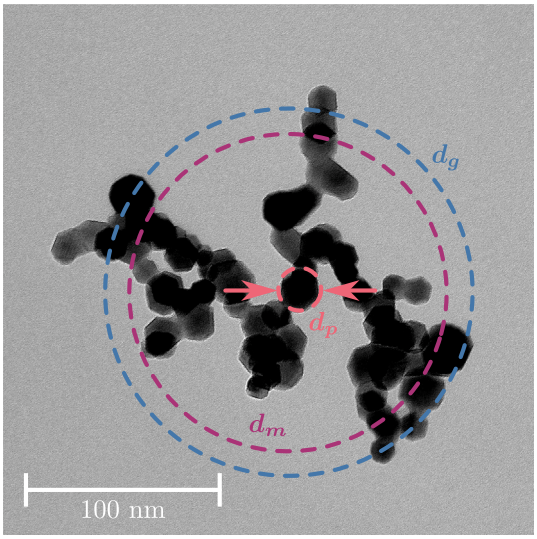

Fig. 2. Iron oxide nanoparticle aggregate with $D_f \approx 1.8$ thermophoretically sampled at a height above burner of 5 cm from an iron dust flame with $\Phi = 1.0$ and $D_{50} = 18.0$ µm. The diameter of gyration d_g, the mobility diameter d_m, and the projected area equivalent primary nanoparticle diameter d_p are indicated.

as shown in [39]. For nanoparticle aggregates, d_m is related to the diameter of gyration d_g [40]. Mackowski derived an empirical relationship between these two quantities for aggregates with $0.7 < D_f < 2.0$ in the free-molecular regime, i.e., $Kn > 1$ [41]:

$$d_g = \left[\frac{d_m}{1.624\, k_f^{\,1-\frac{1}{D_f}}\; {D_f}^{-0.9}\; d_p^{\,1-0.47\,D_f}} \right]^{\frac{1}{0.47\,D_f}} . \tag{3}$$

Following the approach of Kelesidis and Pratsinis [42], the volume fraction of the nanoparticle aerosol can be estimated, accounting for aggregate morphology and considering $P(d_p)$ and $P(d_m)$.

3. Experimental approach

This section introduces the Bunsen-type burner, followed by the investigated flames, sampling positions, on-line mobility sizing, and thermophoretic sampling with electron microscopy. The experimental setup is shown in Fig. 3.

3.1. Iron dust burner of Bunsen-type

In this study, the iron dust burner of Bunsen-type introduced by Fedoryk et al. [22] is employed, enabling the stabilization of self-sustained, laminar iron dust flames without oxygen enrichment, preheating, or cofiring of a gaseous fuel. The setup shown in Fig. 3 uses an air-knife seeder, based on the design by Goroshin et al. [43], to generate an iron dust aerosol. Iron powder is pushed upward through a cylindrical tube by a piston. The oxidizer gas is accelerated through a narrow slit of 30 µm, dispersing the iron particles. This combination of high gas velocity and continuous powder supply generates a stable, ignitable aerosol of micron-sized iron particles. A coflow of air surrounds the outlet tube, shielding the flame. The mass flows of both the coflow and the oxidizer gas, which can be either air or synthetic N_2/O_2 mixtures, are controlled by mass flow controllers (MFCs). Further details of the iron dust burner of Bunsen-type are provided elsewhere [22].

3.2. Investigated iron dust flames of Bunsen-type and sampling positions

In this study, six laminar iron dust flames with a mean outlet velocity of 40 cm s^{-1} were investigated, as summarized in Table 1. The coflow velocity was set to the same value. Fig. 4 shows time-averaged images of the iron dust flames, providing a visual impression. The height above burner (HAB) and the corresponding sampling positions are additionally indicated in Fig. 4.

Flames #1 to #3 enable a comparison of nanoparticle formation and evolution as a function of the equivalence ratio Φ with air serving as the oxidizer. The equivalence ratio is defined with respect to Fe_2O_3, as described in [22]. A comparison of findings from flames #1 and #5 allows conclusions to be drawn regarding the influence of the size distribution of the micron-sized iron particles. The cumulative volume-based particle size distributions, corresponding to the D_{50} values in Table 1, were determined using the method in [44] and are available in the Supplementary Material. The influence of the molar oxygen concentration in the oxidizer is evaluated by studying flames #4 to #6, using iron particles with $D_{50} = 5.5$ µm. By adjusting the number concentration of micron-sized particles in the aerosol, the equivalence ratio is kept constant at $\Phi = 1.0$.

3.3. On-line particle probing and quantification of mobility particle size distribution

The evolution of nanoparticle size distributions in the post-reaction zone of iron dust flames is quantified via on-line particle sizing. This subsection outlines the aerosol probe and sampling system, the separation of micron- and nano-sized particles using an impaction stage, and differential mobility sizing.

3.3.1. Aerosol probe and sampling system

For differential mobility sizing, the aerosol probe introduced by Zhao et al. [45] is employed, enabling on-line sampling and sizing of flame-made nanoparticles. As shown in Fig. 3, a horizontally aligned, 3D-traversable ceramic tube with an inner diameter of 8.55 mm and a wall thickness of 700 µm, featuring a lateral orifice of 300 µm oriented toward the flame, is positioned at defined HABs within the investigated iron dust flames. Through the orifice, particle-laden flame gas is extracted by applying a controlled pressure drop of 700 Pa using a vacuum pump. Upon entering the probe, the aerosol is diluted within approx. 100 µs with nitrogen at 300 K and a flow rate of 30 l min^{-1}, resulting in a dilution ratio f_D of $> 5\times10^3$. This quenches oxidation reactions and prevents coagulation during the short transport time. A secondary dilution step further reduces the number concentration before the aerosol is split: 1.5 l min^{-1} is directed to the impaction stage and differential mobility sizing, see Section 3.3.2, while the remainder is exhausted. The dilution ratio allows calculating the absolute particle number concentration per mobility size as $N_m(d_m) = f_D\, N'_m(d_m)$, where $N'_m(d_m)$ is the measured number concentration per mobility size. $N'_m(d_m)$ is corrected for particle losses in the probing system as described in [39,46]. The determination of f_D follows the approach of [45]. For the nanoparticle-laden flame aerosol, we assume a constant gas-phase temperature of 1600 K, which was selected as a reasonable estimate for the maximum gas-phase temperature at the flame tip, guided by numerical simulations of laminar iron dust flames of Bunsen-type [47]. Even when assuming a large deviation of ±300 K, the resulting uncertainty of $< \pm 30$ % in f_D, remains comparable to the uncertainty estimated by Frenzel et al. [48]. Note that underestimating the gas-phase temperature overestimates f_D and thus underestimates $N_m(d_m)$, and *vice versa*. Since higher gas-phase temperatures promote nanoparticle formation but also increase the dilution factor f_D, the true nanoparticle number concentration $N_m(d_m)$ is likely underestimated at elevated temperatures. As the degree of underestimation scales with temperature, the observed trends are likely even more pronounced once accurate temperature fields are considered. Spatially resolved measurements of gas-phase temperatures - beyond the scope of this work but addressed in future work—will reduce the uncertainty and enable recursive corrections to f_D and, consequently, $N_m(d_m)$.

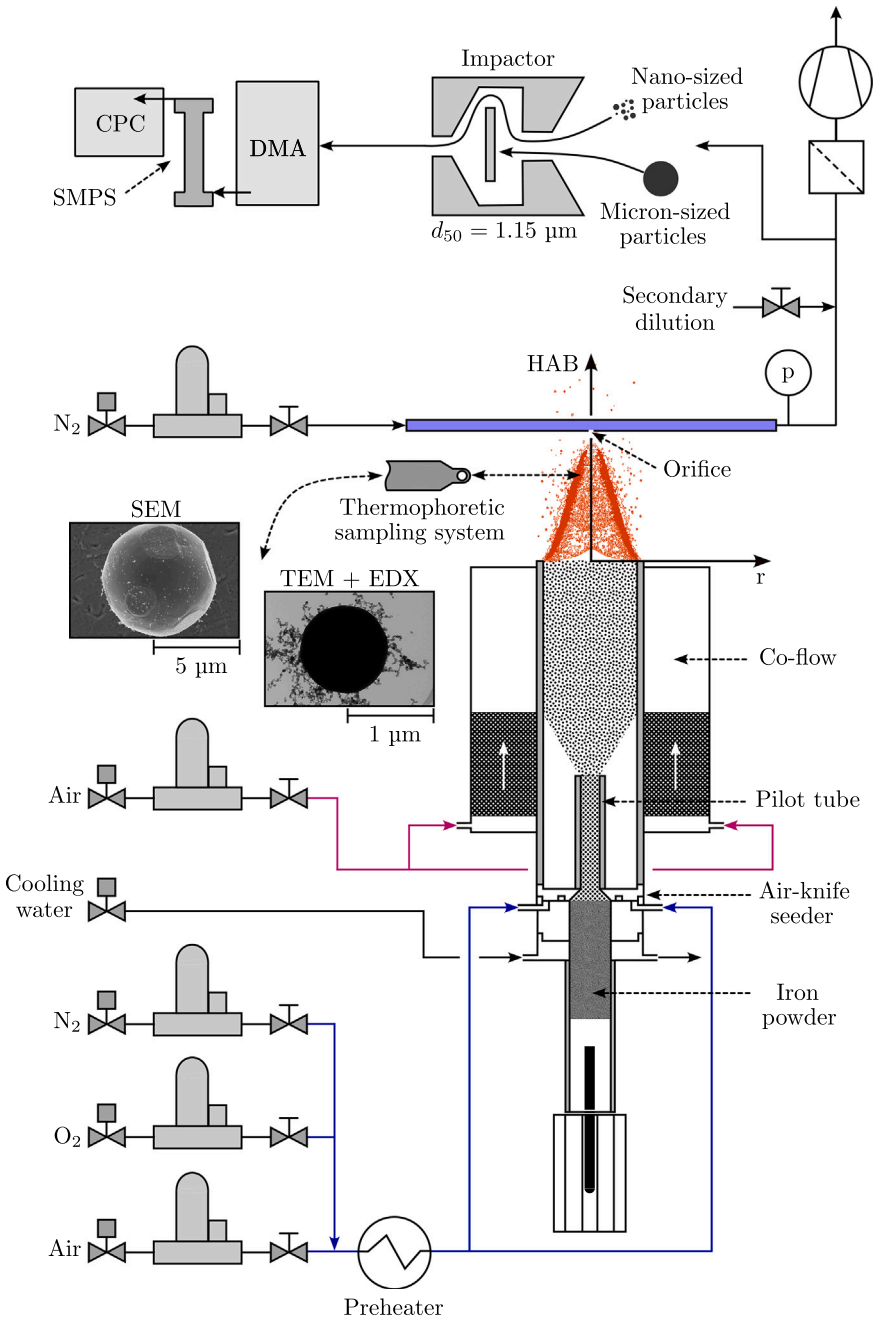

Fig. 3. Experimental setup including the iron dust burner of Bunsen-type, on-line particle probing system coupled to impactor, differential mobility analyzer (DMA) and condensation particle counter (CPC), as well as the thermophoretic sampling system used to collect micron- and nano-sized particles for scanning and transmission electron microscopy (SEM and TEM) and energy-dispersive X-ray (EDX) analysis.

3.3.2. Micron- and nano-sized particle separation and differential mobility sizing

The diluted aerosol sampled from the iron dust flames, consisting of micron-sized particles, hetero- and nanoparticle aggregates as well as single nanoparticles, is directed into an impactor, see Fig. 3. The impactor aerodynamically separates particles based on their inertia. micron-sized particles and hetero-aggregates with a high Stokes number impact on a plate, while nanoparticles and/or nanoparticle aggregates with a low Stokes number follow the gas flow, allowing selective analysis of micron- and nano-sized particles. The cut-off size of the impactor at the given flow rate of 1.5 l min^{-1} is d_{50} = 1.15 µm.

The nanoparticle aerosol then enters a Scanning Mobility Particle Sizer (SMPS). First, soft X-rays neutralize the particles by ionizing air molecules, establishing a bipolar charge equilibrium according to the Fuchs theory [49]. This charge conditioning is critical, as the electrical mobility of nanoparticles and aggregates—and thus their size classification—depends on the charge state. Subsequently, the Differential Mobility Analyzer (DMA) classifies particles based on their electrical mobility Z_p, which is inversely proportional to particle size for a given charge [50]:

$$Z_p = \frac{e\,C_c}{3\,\pi\,\eta\,d_m}. \tag{4}$$

Here, e is the elementary charge, C_c the Cunningham slip correction factor [46], η the gas viscosity, and d_m the mobility size as defined in sec. 2. Smaller particles exhibit higher mobilities, as their lower drag allows

Table 1
Investigated laminar iron dust flames of Bunsen-type with a mean outlet velocity of 40 cm s^{-1}.

Flame	Φ/–	D_{50}/μm	$[O_2]$/vol.-%
#1	0.80	18.0	21
#2	1.00	18.0	21
#3	1.25	18.0	21
#4	1.00	5.5	19
#5	1.00	5.5	21
#6	1.00	5.5	25

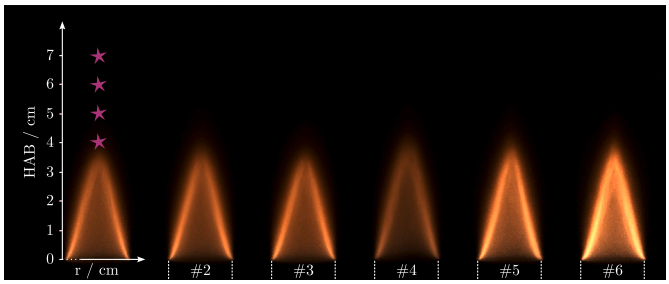

Fig. 4. Time-averaged images of the laminar iron dust flames investigated in this study, as listed in Table 1. Sampling positions are also indicated. Flames #1 to #3 represent an increasing equivalence ratio Φ from 0.80 to 1.00 and 1.25, with D_{50} = 18.0 μm. Flames #4 to #6 correspond to an increasing molar oxygen concentration in the oxidizer from 19 vol.-% to air and 25 vol.-%, with Φ = 1.00 and D_{50} = 5.5 μm. Minor differences in flame height due to variations in laminar flame speed exist but are not clearly discernible in the images.

faster movement in an electric field. For size classification in the DMA, nanoparticles and aggregates are introduced into an annular region between two electrodes, with only those having Z_p corresponding to the applied voltage traversing the DMA and reaching the detector, i.e., a Condensation Particle Counter (CPC). In the CPC, particles from the diluted aerosol are exposed to a supersaturated n-butanol vapor, which condenses on their surface, leading to rapid growth into micron-sized droplets. These droplets are counted via light scattering. Combining size classification of the aerosol and the quantification of the number concentration of size-selected fractions yields the number size distribution $\mathrm{d}N_m/\mathrm{d}\log(d_m)$, representing the number concentration per logarithmic interval of the mobility diameter. In this study, $\mathrm{d}N_m/\mathrm{d}\log(d_m)$ is then approximated by a log-normal fit to derive $P(d_m)$ and thus to determine $\overline{d}_m$ and $\sigma_{g,m}$.

In this study, a Long DMA (TSI Model 3081A) with an aerosol flow rate of 1.5 l min^{-1} is used, covering a size range of d_m = 7 … 200 nm. Initial tests with a Nano DMA (TSI Model 3085A), which operates in the range d_m = 1 … 70 nm, indicated that the particle number concentration below 7 nm is negligible, whereas a significant fraction of particles exceeds 70 nm, as shown later. Further details on the instrumentation, including the soft X-ray source and CPC, are provided elsewhere [39,51].

3.4. Thermophoretic particle sampling and characterization via electron microscopy

A thermophoretic sampling system was employed to collect micron- and nano-sized particles for subsequent morphological and elemental analysis. This subsection details the thermophoretic sampling system, along with SEM, TEM, and EDX spectroscopy for particle analysis. Image analysis methods for determining the nanoparticle size distribution $P(d_p)$ and the fractal dimension D_f of aggregates are introduced.

3.4.1. Thermophoretic sampling system

Micron- and nano-sized particles were thermophoretically sampled at the positions shown in Fig. 4 using copper grids with a diameter of 3.05 mm and a thin carbon film coating of ≤3 nm. An electromagnetic fast-insertion system positioned the grid at the desired axial location in the iron dust flames and/or post-flame region. The design of the grid holder used in this study was introduced by Altenhoff et al. [52]. A residence time of 200 ms at the sampling position proved effective, while insertion and retraction times were below 10 ms. This approach yielded a suitable particle loading for electron microscopy without causing visible distortion of the flames.

3.4.2. Scanning electron microscopy

The morphology of hetero-aggregates and combusted micron-sized particles was investigated as a function of HAB using SEM. The sampled grids were examined with a LEO 1530 Gemini, equipped with a Schottky field emitter and operated at 5 kV acceleration voltage.

3.4.3. Transmission electron microscopy, energy-dispersive X-ray spectroscopy and image analysis methods

Both the morphology of hetero-aggregates and the chemical composition of nanoparticles sampled on the grids were analyzed using a Thermo Fisher Scientific Tecnai Osiris TEM. The system is equipped with an X-FEG high-brightness Schottky field emission gun, operated at 200 kV, and an EDX detector. EDX spectroscopy was employed to identify the iron oxide phase of nanoparticles via elemental mapping of oxygen and iron.

A representative TEM image of an aggregate is shown in Fig. 2. TEM images were analyzed to determine structural properties not accessible via mobility sizing, specifically the size distribution of nanoparticles forming the aggregates $P(d_p)$ and the fractal dimension D_f of the aggregates. In this study, D_f was estimated using the Modified Box-Counting (MBC) method following Wozniak et al. [53]. $P(d_p)$ was evaluated based on the projected area equivalent diameter [54].

4. Results and discussion

This section first discusses the evolution of the nanoparticle size distribution and the impact of hetero-coagulation for flame #2, followed by an analysis of how the equivalence ratio, micron-sized iron particle size distribution, and oxygen concentration in the oxidizer influence these processes.

Preliminary non-reactive experiments with aerosols of micron-sized particles were conducted to determine the fraction of nanoparticles in the uncombusted iron powder. For the iron particle system with D_{50} = 18.0 μm, the fraction of nano-sized particles relative to the number concentration of flame-made nanoparticles was below 1 % in the stoichiometric iron dust flame with air as the oxidizer, see flame #2. For the comparable flame #5 with D_{50} = 5.5 μm, this fraction was <0.5 %.

4.1. Evolution of nanoparticle size distribution and hetero-coagulation with micron-sized particles

The evolution of the nanoparticle size distribution along the flame axis and the impact of hetero-coagulation are analyzed for the stoichiometric iron dust flame with D_{50} = 18 μm, flame #2, see Table 1.

In the reaction zone of the iron dust flame, nanoparticles form in the boundary layer of the burning micron-sized particles. Their transport into the surrounding gas phase is likely governed by thermophoresis and, depending on particle temperature, Stefan flow, as explained in Section 2 or [19]. Downstream of the reaction zone, i.e., at HAB = 4 cm, nanoparticles of 2 … 50 nm in size are found, exhibiting a $P(d_p)$ with a CMD of approximately 23 nm, as shown in Fig. 5. The analyzed nanoparticles appear both as free spheres and in aggregates, as visible in Fig. 6. With increasing HAB, i.e., residence time, surface growth is observed, most likely driven by condensation. The size distribution $P(d_p)$ shifts toward larger diameters and becomes broader with increasing HAB. This behavior is representative and has been observed for all investigated iron dust flames.

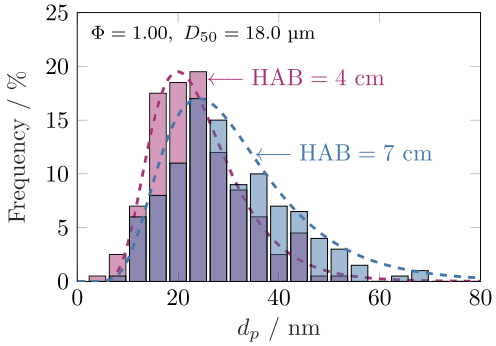

Fig. 5. Nanoparticle size distributions $P(d_p)$ determined from TEM images based on the projected area equivalent diameter. At HAB = 4 cm of flame #2, $\overline{d}_p$ = 22.9 nm and $\sigma_{g,p}$ = 1.45 are quantified. With increasing HAB, nanoparticles grow in size, resulting in $\overline{d}_p$ = 28.9 nm and $\sigma_{g,p}$ = 1.53. Each distribution is based on the analysis of more than 200 nanoparticles.

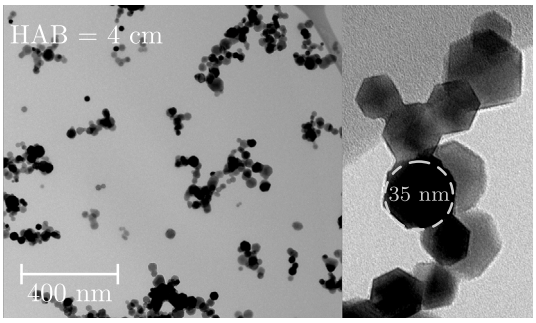

Fig. 6. TEM image on the left shows single nanoparticles and fractal aggregates thermophoretically sampled at HAB = 4 cm in flame #2. On the right, a magnification of an aggregate reveals non-spherical, irregular, and edgy nanoparticles.

Despite uncertainties in quantitative phase analysis via EDX mapping, thermophoretically sampled nanoparticles are identified as Fe_2O_3, consistent with [5,12,14,16]. This is further supported by their non-spherical, irregular, and edgy shape, indicating γ-Fe_2O_3 [55]. Based on the observed nanoparticle morphology, no phase transition from metastable cubic γ-Fe_2O_3 to thermodynamically stable α-Fe_2O_3 is observed, likely due to the short residence times within the flame. Similar observations have been reported for spray flame synthesis of iron oxide nanoparticles [56]. Note that the oxide phase of nanoparticles near a burning micron-sized particle may differ; however, this is not necessarily the case at the investigated HABs downstream of the reaction zone.

At HAB = 4 cm, fractal dimensions ranging from 1.4 to 2.0 are found, with the vast majority of aggregates exhibiting $D_f \approx 1.8$. This suggests that diffusion-limited cluster-cluster agglomeration is the dominant formation mechanism, leading to open, fractal aggregate structures, as shown in Fig. 6. At HAB = 7 cm, single spheres are almost entirely absent, indicating that most nanoparticles have either coagulated with other nanoparticles and/or aggregates into (larger) aggregates or formed hetero-aggregates with micron-sized particles. The fractal dimension of free aggregates remains unchanged along the flame axis, indicating a consistent aggregation mechanism. However, large superaggregates with sizes of several micrometers are frequently observed, indicating progressive coagulation of smaller aggregates. An exemplary TEM image illustrating this observation is provided in the Supplementary Material.

At HAB = 4 cm, just above the flame tip, hetero-coagulation begins between the formed nanoparticles and micron-sized particles.

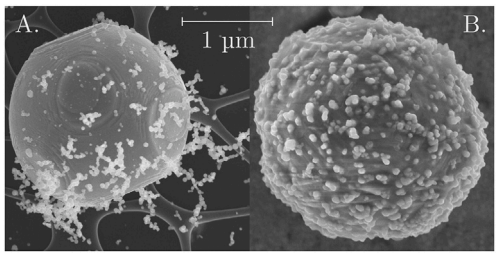

Fig. 7. SEM images of two types, A and B, of micron-sized particles with nanoparticles hetero-coagulated and attached to its surface, thermophoretically sampled at HAB = 4 cm in flame #2.

Notably, two types of hetero-aggregates are observed, as shown in Fig. 7.

Type A, the predominant hetero-aggregate, is shown on the left in Fig. 7. It features micron-sized particles with smooth surfaces on which nanoparticles and aggregates are deposited. Electron microscopy does not clearly indicate whether these deposits are firmly bonded via sintering bridges or merely loosely attached. However, the continuous growth of the nanoparticle mesh on the surface of micron-sized particles suggests that the bonding is not entirely loose. Nanoparticles or aggregates from the surrounding gas phase likely hetero-coagulate with the micron-sized particles and may subsequently sinter at high gas temperatures.

The evolution of hetero-aggregate type A along the flame axis is shown in Fig. 8. Corresponding SEM images are provided in the Supplementary Material. The number of nanoparticles deposited on the micron-sized particles steadily increases. Due to the fractal structure of the deposited nanoparticle aggregates, the surrounding nanoparticle mesh expands with increasing HAB. Consequently, the surface area of the formed hetero-aggregate available for coagulation and deposition continues to increase. At HAB = 7 cm, the TEM image shows an extensive nanoparticle mesh surrounding the micron-sized particle, see Fig. 8.

A micron-sized particle of type B is shown on the right in Fig. 7. This type appears less frequently among the particles analyzed via SEM. Its surface is rough and irregular, suggesting that nano-sized particles have fused with it. One possible explanation is that nanoparticles or their aggregates deposit onto the molten surface of the micron-sized particle, which then solidifies before the nanoparticles fully dissolve into the melt.

Fig. 9 shows the size distributions determined via on-line particle probing and differential mobility sizing along the flame axis. The corresponding $\overline{d}_m$, $\sigma_{g,m}$, and number concentration N_m, derived from log-normal fits of $P(d_m)$ to the experimental data, are presented in Fig. 10. At HAB = 4 cm, the highest particle number concentration is observed, with a CMD of approx. 53 nm. Considering $P(d_p)$ shown in Fig. 5, part of the mobility size distribution can be attributed to single gas-borne nanoparticles, while the rest corresponds to aggregates. With increasing HAB, the CMD of $P(d_m)$ gradually increases, most likely due to coagulation and the formation of larger aggregates. This hypothesis is supported by the decreasing number concentration and the broadening of the size distribution, as indicated by the increasing $\sigma_{g,m}$ values. At HAB = 7 cm, the size distribution exhibits a CMD of approx. 84 nm, while the particle number concentration has decreased by one-third compared to HAB = 4 cm.

By applying the approach proposed by Kelesidis and Pratsinis [42], which accounts for $P(d_p)$ and the fractal morphology of the aggregates, the volume fraction of the nanoparticle aerosol is found to decrease slightly from approximately 2.0 ppm to 1.8 ppm along the flame axis. Although nucleation, growth, and hetero-coagulation occur simultaneously, the observed decrease in volume fraction suggests that hetero-coagulation dominates, reducing the fraction of gas-borne nanoparticles and their aggregates.

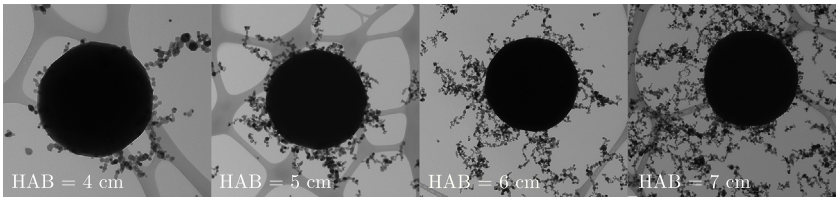

Fig. 8. TEM images of micron-sized particles hetero-coagulated with nanoparticles, thermophoretically sampled along the flame axis of flame #2. From left to right, the particles have sizes of 0.8, 1.2, 1.4, and 1.4 µm. The mesh-like structure in the background corresponds to the carbon film on the copper grid.

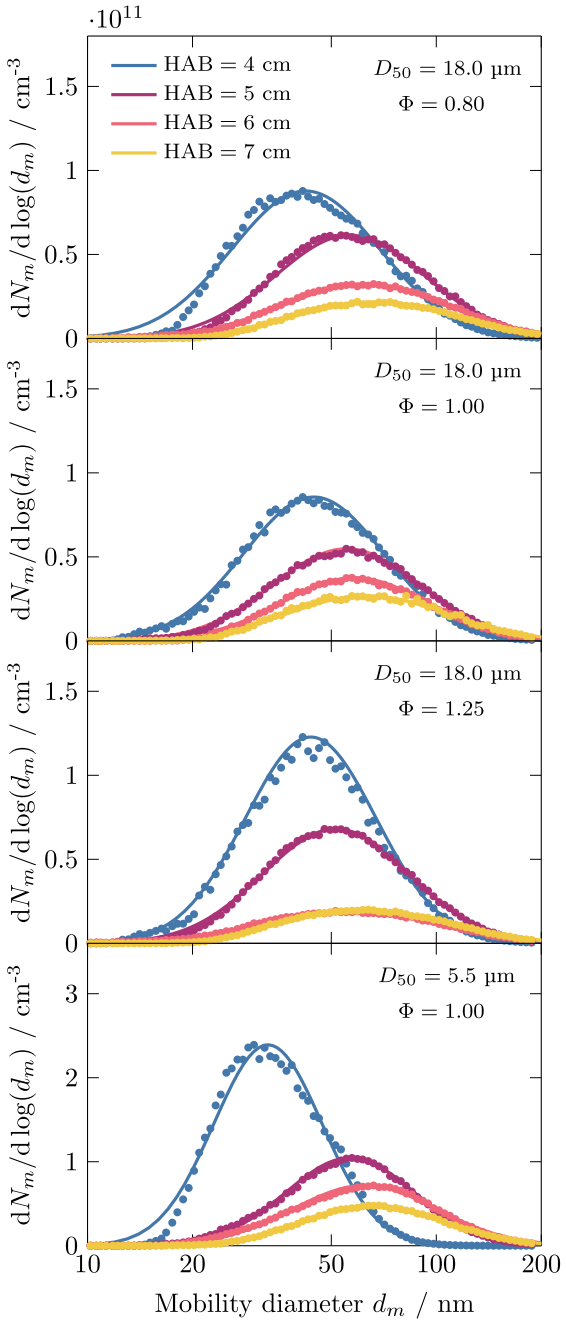

Fig. 9. Number concentration per logarithmic interval of d_m determined via on-line particle probing and differential mobility sizing for flames #1 to #3 and #5. Data points represent measurements, while solid lines indicate the best log-normal fit of $P(d_m)$. Note that the scaling differs for the bottom plot.

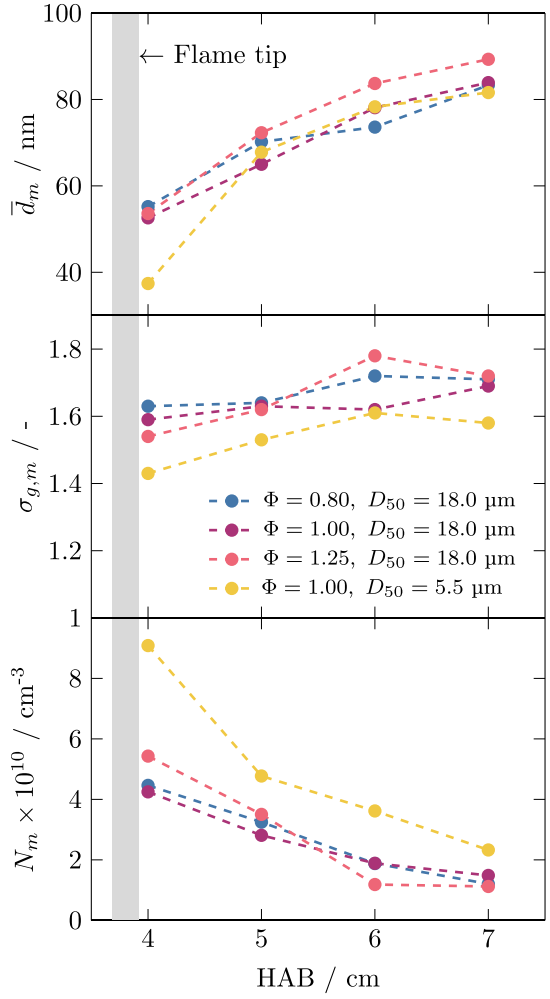

Fig. 10. Count median mobility diameters $\overline{d}_m$, geometric standard deviations $\sigma g, m$, and number concentrations N_m derived from log-normal fits of $P(d_m)$ to the experimental data for flames #1 to #3 and #5, based on the size distributions shown in Fig. 9.

4.2. Influence of equivalence ratio and micron-sized iron particle size distribution

The analysis of $P(d_p)$ and D_f from TEM images reveals that $P(d_p)$ remains largely invariant with varying equivalence ratio, but slightly increases with HAB, as discussed for the stoichiometric flame #2. In contrast, $P(d_m)$ exhibits significant changes along the flame axis, as shown in Figs. 9 and 10. While the CMD of $P(d_m)$ at HAB = 4 cm ranges between 50 … 55 nm, the number concentration N_m increases by approx. 25 % for Φ = 1.25 compared to the stoichiometric flame. This increase reflects the higher mass flow rate of iron for Φ = 1.25,

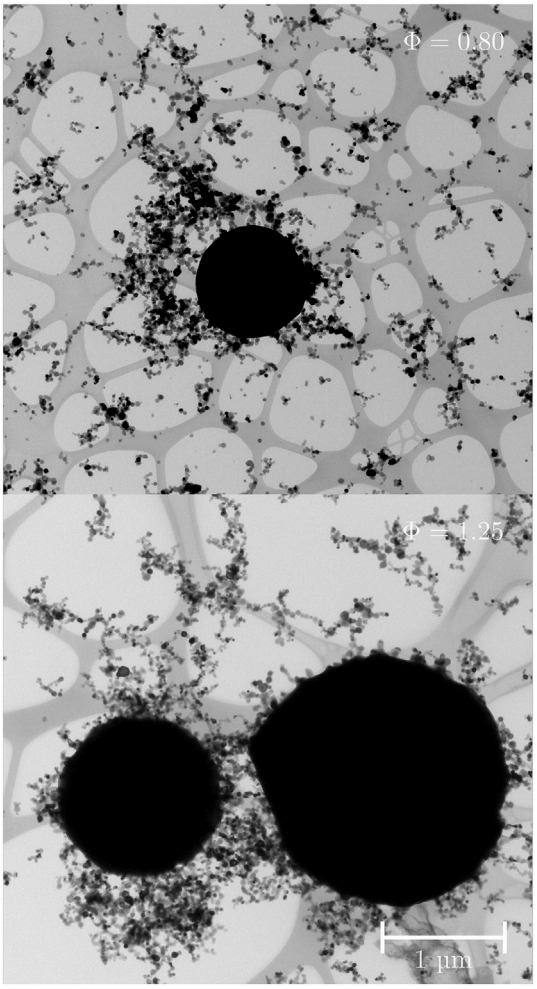

Fig. 11. TEM images of micron-sized particles hetero-coagulated with nanoparticles, thermophoretically sampled at HAB = 7 cm in flames #1 and #3, i.e., Φ = 0.80 and 1.25, respectively. The mesh-like structure in the background corresponds to the carbon film on the copper grid.

indicating that the number of formed nanoparticles scales with the number of seeded micron-sized iron particles. However, from HAB = 4 cm to 7 cm, the volume fraction drops from 2.3 ppm to approx. 1.3 ppm, lower than in the stoichiometric and lean flames. This decrease along the flame axis was attributed to hetero-coagulation between nano- and micron-sized particles in Section 4.1. Since nucleation, condensation, and hetero-coagulation occur simultaneously, the reduction in volume fraction suggests that hetero-coagulation dominates, outweighing the effects of ongoing nanoparticle formation and growth. Given that the iron dust flame with Φ = 1.25 exhibits a 25 % higher number concentration of micron-sized particles, increasing the probability of nanoparticle deposition, this trend seems reasonable.

A first confirmation of this hypothesis is provided in Fig. 11, which shows TEM images of thermophoretically sampled nano- and micron-sized particles at HAB = 7 cm in flames #1 and #3, i.e., Φ = 0.80 and 1.25, respectively. In the lean flame, single uncoagulated nanoparticles and aggregates are present alongside a hetero-aggregate. In contrast, for Φ = 1.25, nanoparticles form a dense nanoparticle mesh surrounding two micron-sized particles.

Reducing the D_{50} of the seeded micron-sized iron particles increases the particle number concentration by roughly a factor of 30. Consequently, both nanoparticle formation and hetero-coagulation are expected to be affected. Consequently, this also implies a reduced interparticle distance, which is expected to affect both nanoparticle

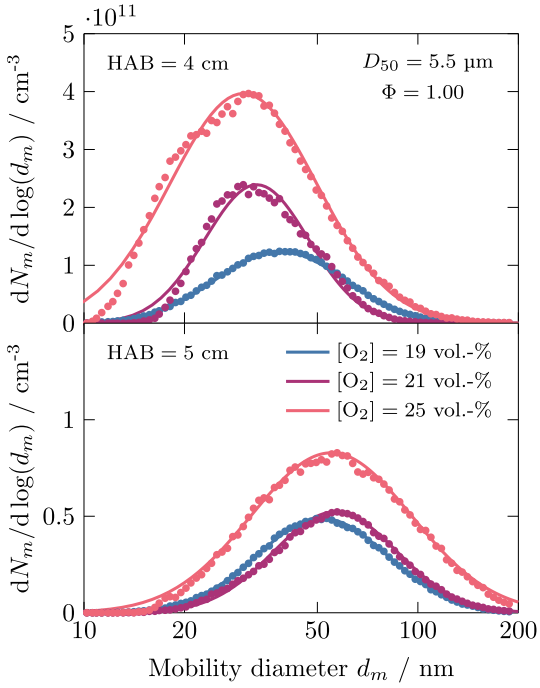

Fig. 12. Number concentration per logarithmic interval of d_m determined via online particle probing and differential mobility sizing at HAB = 4 cm and 5 cm for flames #4 to #6. Data points represent measurements, while solid lines indicate the best log-normal fit of $P(d_m)$. Note that the scaling varies between the plots.

formation and hetero-coagulation. Decreasing D_{50} from 18.0 to 5.5 µm results in a doubling of nanoparticle concentration at the flame tip, i.e., HAB = 4 cm, as shown in Figs. 8 and 10. Simultaneously, the CMD of $P(d_m)$ decreases to approx. 37 nm, while the distribution narrows, i.e., $\sigma_{g,m}$ is lower. The increased N_m is likely a direct consequence of the higher number of burning micron-sized particles, whereas the reduction of the CMD suggests a different formation mechanism for smaller micron-sized particles. The higher number concentration of burning micron-sized particles likely increases the number of nucleation events. However, each micron-sized particle provides only a limited amount of iron (oxide) vapor, reducing growth per incipient nanoparticle, which leads to smaller sizes and narrower distributions. This points to a different formation mechanism: limited vapor availability likely dominates over potential coalescence effects between closely spaced incipient nanoparticles originating from the same micron-sized parent particle.

Following the previously discussed trend, the number concentration N_m decreases by approx. 75 % along the flame axis. The CMD of $P(d_m)$ shifts to the same range as observed for flames #1 to #3 with D_{50} = 18 µm. However, it should be noted that, in contrast to the observed trend for Φ = 1.0 and 1.25 with D_{50} = 18 µm, the increase in nanoparticle number concentration at HAB = 4 cm and its subsequent decrease—likely due to hetero-coagulation—do not scale linearly with the higher number of micron-sized particles when D_{50} is reduced. At HAB = 7 cm, the mobility size distributions appear to converge, consistent with ongoing coagulation dynamics at longer residence times. This observation may be relevant for the design of future nanoparticle capture or filtration strategies.

4.3. Influence of oxygen concentration in the oxidizer

Fig. 12 shows the effect of oxygen concentration in the oxidizer on $P(d_m)$. The observed increase in nanoparticle formation with higher oxygen concentration is consistent with the expected rise in gas-phase temperature, which promotes iron vaporization and subsequent nanoparticle formation [9,10]. These findings are confirmed as the number

concentration more than doubles, while the shape of $P(d_m)$ remains largely unchanged compared to the case of air as the oxidizer, i.e., flame #5. As expected, reducing oxygen suppresses nanoparticle formation. However, at HAB = 5 cm, the number concentration nearly matches that of flame #5, which may be attributed to reduced hetero-coagulation. It must be noted that variations in oxygen concentration may also affect the local Stefan flow in the boundary layer of burning particles, thereby altering the balance of transport processes between thermophoresis and re-entrainment, and thus influencing hetero-coagulation.

Since higher oxygen concentrations likely lead to higher gas-phase temperatures than estimated, the dilution ratio f_D of the aerosol probe is likely overestimated, meaning the actual increase in $P(d_m)$ may be greater than observed, see Section 3.3.1. Conversely, with reduced oxygen, f_D may be underestimated, suggesting that $P(d_m)$ is overestimated.

5. Conclusions

This study investigated the evolution of nanoparticle size distributions in laminar iron dust flames of Bunsen-type, focusing on the interplay between formation, growth, and hetero-coagulation with micron-sized parent particles. The key findings are:

i. **Nanoparticle formation, growth, and evolution in the flame.** Nanoparticles form in the boundary layer of burning micron-sized particles and are subsequently transported into the surrounding gas phase. Their size distribution shifts to larger diameters and broadens along the flame axis due to condensation-driven growth. The mobility size distribution, which includes both single nanoparticles and aggregates, also shifts toward larger sizes along the flame axis. The number concentration decreases due to ongoing coagulation, with hetero-coagulation dominating over further nanoparticle growth, leading to a gradual reduction in the gas-borne nanoparticle volume fraction.
ii. **Hetero-coagulation dynamics.** Two types of hetero-aggregates were identified. The predominant type A consists of micron-sized particles coated with a nanoparticle mesh, which grows continuously along the flame axis. Type B features rough, irregular surfaces, suggesting nanoparticle deposition onto molten surfaces.
iii. **Influence of flame parameters.** The equivalence ratio influences nanoparticle number concentration, with higher equivalence ratio increasing nanoparticle formation at the flame tip. A decrease in micron-sized particle diameter similarly increases nanoparticle number concentration but results in a narrower mobility size distribution. Higher oxygen concentrations further enhance nanoparticle formation by increasing particle temperatures.

These findings indicate that nanoparticle formation in iron dust flames may be mitigated by controlling hetero-coagulation, adjusting the oxygen concentration in the oxidizer, or modifying the equivalence ratio.

CRediT authorship contribution statement

Fabian P. Hagen: Writing – original draft, Visualization, Supervision, Methodology, Investigation, Formal analysis, Conceptualization. **Jonas H. Müller:** Investigation, Formal analysis. **Heike Störmer:** Writing – review & editing, Investigation. **Björn Stelzner:** Writing – review & editing, Supervision. **Yolita M. Eggeler:** Writing – review & editing, Supervision. **Dimosthenis Trimis:** Writing – review & editing, Supervision, Funding acquisition.

Declaration of competing interest

The authors declare that they have no known competing financial interests or personal relationships that could have appeared to influence the work reported in this paper.

Acknowledgments

We thank Volker Zibat and Jonas Kaltenbach from the Laboratory for Electron Microscopy at Karlsruhe Institute of Technology (KIT) for their support and valuable discussions regarding the findings from scanning electron microscopy. Klaus Hirsch, Max P. Deutschmann, and Prof. Dr.-Ing. Hermann Nirschl from the Institute of Mechanical Process Engineering and Mechanics at KIT are acknowledged for measuring the size distributions of the two different iron powders used in the Bunsen-type burner. This work was conducted within the Clean Circles cluster project, supported by the Strategy Fund of the KIT Presidium. Additionally, the research contributes to the Helmholtz Association's MTET program, Resource and Energy Efficiency, Anthropogenic Carbon Cycle (38.05.01).

Supplementary data

Supplementary data to this article can be found online at doi:10.1016/j.fuel.2025.135598.

Data availability

Data will be made available upon request.

References

[1] Bergthorson JM, Goroshin S, Soo MJ, Julien P, Palecka J, Frost DL, et al. Direct combustion of recyclable metal fuels for zero-carbon heat and power. Appl Energy 2015;160:368–82. doi:https://doi.org/10.1016/j.apenergy.2015.09.037.
[2] Bergthorson JM. Recyclable metal fuels for clean and compact zero-carbon power. Prog Energy Combust Sci 2018;68:169–96. doi:https://doi.org/10.1016/j.pecs.2018.05.001.
[3] Debiagi P, Rocha RC, Scholtissek A, Janicka J, Hasse C. Iron as a sustainable chemical carrier of renewable energy: analysis of opportunities and challenges for retrofitting coal-fired power plants. Renew Sust Energy Rev 2022;165:112579. doi:https://doi.org/10.1016/j.rser.2022.112579.
[4] Wronski T, Sciacovelli A. Analysis of the potential of four reactive metals as zero-carbon energy carriers for energy storage and conversion. J Energy Storage 2024;100:113514. doi:https://doi.org/10.1016/j.est.2024.113514.
[5] Poletaev NI, Khlebnikova MY. Combustion of iron particles suspension in laminar premixed and diffusion flames. Combust Sci Technol 2022;194:1356–77. doi:https://doi.org/10.1080/00102202.2020.1812588.
[6] Wang H-C, Kasper G. Filtration efficiency of nanometer-size aerosol particles. J Aerosol Sci 1991;22:31–41. doi:https://doi.org/10.1016/0021-8502(91)90091-U.
[7] Wen D. Nanofuel as a potential secondary energy carrier. Energy Environ Sci 2010;3:591–600. doi:https://doi.org/10.1039/B906384F.
[8] Ning D, Shoshin Y, van Oijen JA, Finotello G, de Goey LPH. Burn time and combustion regime of laser-ignited single iron particle. Combust Flame 2021;230:111424. doi:https://doi.org/10.1016/j.combustflame.2021.111424.
[9] Ning D, Shoshin Y, van Oijen JA, Finotello G, de Goey LPH. Critical temperature for nanoparticle cloud formation during combustion of single micron-sized iron particle. Combust Flame 2022;244:112296. doi:https://doi.org/10.1016/j.combustflame.2022.112296.
[10] Ning D, Shoshin Y, van Stiphout M, van Oijen J, Finotello G, de Goey P. Temperature and phase transitions of laser-ignited single iron particle. Combust Flame 2022;236:111801. doi:https://doi.org/10.1016/j.combustflame.2021.111801.
[11] Li T, Heck F, Reinauer F, Böhm B, Dreizler A. Visualizing particle melting and nanoparticle formation during single iron particle oxidation with multi-parameter optical diagnostics. Combust Flame 2022;245:112357. doi:https://doi.org/10.1016/j.combustflame.2022.112357.
[12] Panahi A, Chang D, Schiemann M, Fujinawa A, Mi X, Bergthorson JM, et al. Combustion behavior of single iron particles-part I: an experimental study in a drop-tube furnace under high heating rates and high temperatures. Appl Energy Combust Sci 2023;13:100097. doi:https://doi.org/10.1016/j.jaecs.2022.100097.
[13] Li S, Sanned D, Huang J, Berrocal E, Cai W, Aldén M, et al. Stereoscopic high-speed imaging of iron microexplosions and nanoparticle-release. Opt Express 2021;29:34465–76. doi:https://doi.org/10.1364/OE.434836.
[14] Tóth P, ögren Y, Sepman A, Gren P, Wiinikka H. Combustion behavior of pulverized sponge iron as a recyclable electrofuel. Powder Technol 2020;373:210–19. doi:https://doi.org/10.1016/j.powtec.2020.05.078.
[15] Thijs LC, van Gool CEAG, Ramaekers WJS, van Oijen JA, de Goey LPH. Resolved simulations of single iron particle combustion and the release of nano-particles. Proc Combust Inst 2023;39:3551–59. doi:https://doi.org/10.1016/j.proci.2022.07.044.
[16] Palečka J, Sniatowsky J, Goroshin S, Higgins AJ, Bergthorson JM. A new kind of flame: observation of the discrete flame propagation regime in iron particle suspensions in microgravity. Combust Flame 2019;209:180–86. doi:https://doi.org/10.1016/j.combustflame.2019.07.023.
[17] Li T, Nguyen B-D, Gao Y, Ning D, Böhm B, Scholtissek A, et al. Critical nanoparticle formation in iron combustion: single particle experiments with in-situ multi-parameter diagnostics aided by multi-scale simulations, Preprint.

[18] van Gool CEAG, Thijs LC, Ramaekers WJS, van Oijen JA, de Goey LPH. Particle equilibrium composition model for iron dust combustion. Appl Energy Combust Sci 2023;13:100115. doi:https://doi.org/10.1016/j.jaecs.2023.100115.
[19] Nguyen B-D, Scholtissek A, Li T, Ning D, Stein OT, Dreizler A, et al. Nanoparticle formation in the boundary layer of burning iron microparticles: modeling and simulation. Chem Eng J 2025;507:160039. doi:https://doi.org/10.1016/j.cej.2025.160039.
[20] Li T, Farmand P, Geschwindner C, Greifenstein M, Köser J, Schumann C, et al. Homogeneous ignition and volatile combustion of single solid fuel particles in air and oxy-fuel conditions. Fuel 2021;291:120101. doi:https://doi.org/10.1016/j.fuel.2020.120101.
[21] Buchheiser S, Deutschmann MP, Rhein F, Allmang A, Fedoryk M, Stelzner B, et al. Particle and phase analysis of combusted iron particles for energy storage and release. Materials 2023;16:2009. doi:https://doi.org/10.3390/ma16052009.
[22] Fedoryk M, Stelzner B, Harth S, Trimis D. Experimental investigation of the laminar burning velocity of iron-air flames in a tube burner. Appl Energy Combust Sci 2023;13:100111. doi:https://doi.org/10.1016/j.jaecs.2022.100111.
[23] Friedlander SK, Windeler RS, Weber AP. Ultrafine particle formation by aerosol processes in turbulent jets: mechanisms and scale-up. Nanostruct Mater 1994;4:521–28. doi:https://doi.org/10.1016/0965-9773(94)90059-0.
[24] Wlokas I, Faccinetto A, Tribalet B, Schulz C, Kempf A. Mechanism of iron oxide formation from iron pentacarbonyl-doped low-pressure hydrogen/oxygen flames. Int J Chem Kinet 2013;45:487–98. doi:https://doi.org/10.1002/kin.20786
[25] Feder J, Russell KC, Lothe J, Pound GM. Homogeneous nucleation and growth of droplets in vapours. Adv Phys 1966;15:111–78. doi:https://doi.org/10.1080/00018736600101264.
[26] Freund HJ, Bauer SH. Homogeneous nucleation in metal vapors. 2. Dependence of the heat of condensation on cluster size. J Phys Chem 1977;81:994–1000. doi:https://doi.org/10.1021/j100525a014.
[27] Warren DR, Seinfeld JH. Nucleation and growth of aerosol from a continuously reinforced vapor. Aerosol Sci Technol 1984;3:135–53. doi:https://doi.org/10.1080/02786828408959003.
[28] Finke J, Sewerin F. Combining a population balance approach with detailed chemistry to model the condensation of oxide smoke during aluminum combustion in spatially homogeneous reactors. Combust Flame 2023;248:112510. doi:https://doi.org/10.1016/j.combustflame.2022.112510.
[29] Wooldridge MS. Gas-phase combustion synthesis of particles. Prog Energy Combust Sci 1998;24:63–87. doi:https://doi.org/10.1016/S0360-1285(97)00024-5.
[30] Finke J, Sewerin F. An unsteady PBE-CFD analysis of the asymmetric smoke-laden flame around a burning aluminum particle. Proc Combust Inst 2024;40:105564. doi:https://doi.org/10.1016/j.proci.2024.105564.
[31] Landgrebe JD, Pratsinis SE. Gas-phase manufacture of particulates: interplay of chemical reaction and aerosol coagulation in the free-molecular regime. Ind Eng Chem Res 1989;28:1474–81. doi:https://doi.org/10.1021/ie00094a007.
[32] Heintzenberg J. Properties of the log-normal particle size distribution. Aerosol Sci Technol 1994;21:46–48. doi:https://doi.org/10.1080/02786829408959695.
[33] Kelesidis GA, Goudeli E, Pratsinis SE. Flame synthesis of functional nanostructured materials and devices: surface growth and aggregation. Proc Combust Inst 2017;36:29–50. doi:https://doi.org/10.1016/j.proci.2016.08.078.
[34] Sun J, Simon SL. The melting behavior of aluminum nanoparticles. Thermochim Acta 2007;463:32–40. doi:https://doi.org/10.1016/j.tca.2007.07.007.
[35] Meierhofer F, Fritsching U. Synthesis of metal oxide nanoparticles in flame sprays: review on process technology, modeling, and diagnostics. Energy Fuels 2021;35:5495–537. doi:https://doi.org/10.1021/acs.energyfuels.0c04054.
[36] Sorensen CM, Roberts GC. The prefactor of fractal aggregates. J Colloid Interface Sci 1997;186:447–52. doi:https://doi.org/10.1006/jcis.1996.4664.
[37] Schaefer DW, Hurd AJ. Growth and structure of combustion aerosols: fumed silica. Aerosol Sci Technol 1990;12:876–90. doi:https://doi.org/10.1080/02786829008959400.
[38] Eggersdorfer ML, Pratsinis SE. The structure of agglomerates consisting of polydisperse particles. Aerosol Sci Technol 2012;46:347–53. doi:https://doi.org/10.1080/02786826.2011.631956.
[39] Hagen FP, Vlavakis P, Seitz M, Klövekorn T, Bockhorn H, Suntz R, et al. Soot nanoparticle sizing in counterflow flames using in-situ particle sampling and differential mobility analysis verified with two-color time-resolved laser-induced incandescence. Proc Combust Inst 2023;39:1119–28.
[40] Sorensen CM. The mobility of fractal aggregates: a review. Aerosol Sci Technol 2011;45:765–79. doi:https://doi.org/10.1080/02786826.2011.560909.
[41] Mackowski DW. Monte Carlo simulation of hydrodynamic drag and thermophoresis of fractal aggregates of spheres in the free-molecule flow regime. J Aerosol Sci 2006;37:242–59. doi:https://doi.org/10.1016/j.jaerosci.2004.11.011.
[42] Kelesidis GA, Pratsinis SE. Determination of the fraction of soot accounting for its composition and morphology. Proc Combust Inst 2021;38:1189–96. doi:https://doi.org/10.1016/j.proci.2020.07.055.
[43] Goroshin S, Bidabadi M, Lee JHS. Quenching distance of laminar flame in aluminum dust clouds. Combust Flame 1996;105:147–60. doi:https://doi.org/10.1016/0010-2180(95)00183-2.
[44] Deutschmann MP, Sperling A, Covini E, Böhm B, Dreizler A, Nirschl H. Single iron particle combustion - a morphology study of partially oxidized iron particles. Powder Technol 2024;445:120102. doi:https://doi.org/10.1016/j.powtec.2024.120102.
[45] Zhao B, Yang Z, Wang J, Johnston MV, Wang H. Analysis of soot nanoparticles in a laminar premixed ethylene flame by scanning mobility particle sizer. Aerosol Sci Technol 2003;37:611–20. doi:https://doi.org/10.1080/02786820300908.
[46] Hinds WC. Aerosol technology: properties, behavior, and measurement of airborne particles. John Wiley & Sons, Inc.; 1999.
[47] Hazenberg T, Braig D, Fedoryk MA, Mich J, Hagen FP, Harth SR, et al. Analyzing iron dust bunsen flames using numerical simulations, arXiv preprint arXiv:2503.20692.
[48] Frenzel I, Krause H, Trimis D. Study on the influence of ethanol and butanol addition on soot formation in iso-octane flames. Energy Procedia 2017;120:721–28. doi:https://doi.org/10.1016/j.egypro.2017.07.203.
[49] Fuchs NA. On the stationary charge distribution on aerosol particles in a bipolar ionic atmosphere. Geofis Pura Appl 1963;56:185–93. doi:https://doi.org/10.1007/BF01993343.
[50] Wang SC, Flagan RC. Scanning electrical mobility spectrometer. Aerosol Sci Technol 1990;13:230–40. doi:https://doi.org/10.1080/02786829008959441.
[51] Hagen FP, Rinkenburger A, Günther J, Bockhorn H, Niessner R, Suntz R, et al. Spark discharge-generated soot: varying nanostructure and reactivity against oxidation with molecular oxygen by synthesis conditions. J Aerosol Sci 2020;143:105530. doi:https://doi.org/10.1016/j.jaerosci.2020.105530.
[52] Altenhoff M, Teige C, Storch M, Will S. Novel electric thermophoretic sampling device with highly repeatable characteristics. Rev Sci Instrum 2016;87:125108. doi:https://doi.org/10.1063/1.4971988.
[53] Wozniak M, Onofri FRA, Barbosa S, Yon J, Mroczka J. Comparison of methods to derive morphological parameters of multi-fractal samples of particle aggregates from tem images. J Aerosol Sci 2012;47:12–26. doi:https://doi.org/10.1016/j.jaerosci.2011.12.008.
[54] Hagen FP, Bockhorn H, Störmer H, Loukou A, Suntz R, Trimis D. Nanostructural and morphological characteristics of single soot aggregates during low-temperature oxidation. Proc Combust Inst 2021;38:1153–61. doi:https://doi.org/10.1016/j.proci.2020.06.338.
[55] Li D, Teoh WY, Selomulya C, Woodward RC, Munroe P, Amal R. Insight into microstructural and magnetic properties of flame-made γ-Fe_2O_3 nanoparticles. J Mater Chem 2007;17:4876–84. doi:https://doi.org/10.1039/B711705A.
[56] Tischendorf R, Simmler M, Weinberger C, Bieber M, Reddemann M, Fröde F, et al. Examination of the evolution of iron oxide nanoparticles in flame spray pyrolysis by tailored in situ particle sampling techniques. J Aerosol Sci 2021;154:105722. doi:https://doi.org/10.1016/j.jaerosci.2020.105722.